MRS Communications (2019), *9*, 1221–1226
© Materials Research Society, 2019
doi:10.1557/mrc.2019.137

MRS Communications

Research Letter

Dual light-emitting Yb^{3+},Er^{3+}-doped $La(IO_3)_3$ iodate nanocrystals: up-conversion and second harmonic generation

Sylvain Regny, Univ. Grenoble Alpes, CNRS, Grenoble INP, Institut Néel, F-38000 Grenoble, France
Kévin Bredillet and **Jérémy Riporto,** Univ. Savoie Mont Blanc, SYMME, F-74000 Annecy, France
Isabelle Gautier-Luneau, Univ. Grenoble Alpes, CNRS, Grenoble INP, Institut Néel, F-38000 Grenoble, France
Yannick Mugnier and **Ronan Le Dantec,** Univ. Savoie Mont Blanc, SYMME, F-74000 Annecy, France
Géraldine Dantelle, Univ. Grenoble Alpes, CNRS, Grenoble INP, Institut Néel, F-38000 Grenoble, France
Address all correspondence to Géraldine Dantelle at **geraldine.dantelle@neel.cnrs.fr**

(Received 18 July 2019; accepted 27 September 2019)

Abstract

The authors report the microwave-assisted hydrothermal synthesis of α-$La(IO_3)_3$ nanocrystals doped with Yb^{3+} and Er^{3+} ions, along with their structural and optical characterizations. 50-nm-sized α-$La_{0.9-x}Yb_{0.1}Er_x(IO_3)_3$ nanocrystals with $x = 0.005$, 0.01, and 0.02 were synthesized and dispersed in ethylene glycol. The as-obtained suspensions exhibit both second harmonic generation (SHG) signal and up-conversion photoluminescence (UC-PL) without interplay between the two signals under near-infrared resonant excitation. The relative intensity of SHG and UC-PL emission can be modulated according to the excitation wavelength. The most intense UC-PL signal is obtained from a 980-nm excitation, thanks to the sensitization of Er^{3+} by Yb^{3+}.

Introduction

With the advent of nanotechnologies and nanomedicine, numerous fluorescent optical nanoprobes have been designed for in vitro, ex vivo, and in vivo bio-imaging, such as dye-doped silica nanoparticles,[1] rare earth-doped nanocrystals,[2] and nanodiamonds[3] as recently reviewed.[4] For in vivo experiments, the penetration depth is a crucial parameter[5] and the use of emitters with excitation properties in the near-infrared (NIR) region and the so-called biologic transparency windows (BWs) is required. Based on down-conversion fluorescence, Nd^{3+}-doped fluorescence probes[6,7] or more complex multi-doped architectures[8,9] have raised high interest with their excitation at 808 nm and their emission in the first (750–950 nm), second (1000–1350 nm), and third (1500–1800 nm) BWs, ensuring deep tissue imaging while minimizing tissue autofluorescence and photon scattering. Similarly, PbS or InP quantum dots appear as good candidates for biologic applications thanks to their tunable NIR emission.[10] Among other recent developments, the use of nanoprobes excited through a two-photon process has also been studied, allowing an excitation in the BWs and resulting in a higher spatial selectivity than the one-photon down-conversion fluorescence, as the emission only occurs at the focal point of the excitation laser. Up-conversion photoluminescence (UC-PL), two-photon excitation fluorescence, and second harmonic generation (SHG) are the different envisioned processes. The latter, characterized by transitions from virtual levels, offers the advantage of a tunable excitation in the material transparency range and in the different BWs.

To benefit from the advantages of the different fluorescence-based and nonlinear optical (NLO) imaging techniques, bimodal nanoprobes were recently introduced.[11] For instance, UC-PL and SHG-active nanoprobes would allow to combine the advantages of both processes: PL can be easily detected using conventional microscopy platforms but is a slow process (typical excited-state lifetimes for rare earth emitters are of the order of tens of μs to ms), whereas NLO imaging from harmonic nanoparticles (HNPs)[12,13] is less implemented on commercial microscopes. SHG and third harmonic generation (THG) signals are polarization-sensitive, instantaneous processes and their simultaneous acquisition results in rapid two-dimensional scans and a better imaging selectivity in demanding applications.[14] In addition, SHG- and THG-active nanoprobes do not evidence any blinking, photobleaching, or saturation process, allowing prolonged studies.[15,16] However, only a very limited number of nanosources producing both SHG and UC-PL have been reported in the literature[11] due to the difficulty to find a single-phase nanomaterial that is both non-centrosymmetric and a good host for luminescent species.

Acentric α-$La(IO_3)_3$ is known for its SHG activity as initially demonstrated from comparative micron-sized powder experiments.[17,18] Recently, we reported the synthesis of α-$La(IO_3)_3$ nanocrystals and the quantitative assessment of its orientation-averaged SHG efficiency[19] that was found comparable to the other HNPs of interest (KTP, $BaTiO_3$, $LiNbO_3$, etc.).[20,21] We also evidenced the possibility of doping α-La

https://doi.org/10.1557/mrc.2019.137 Published online by Cambridge University Press

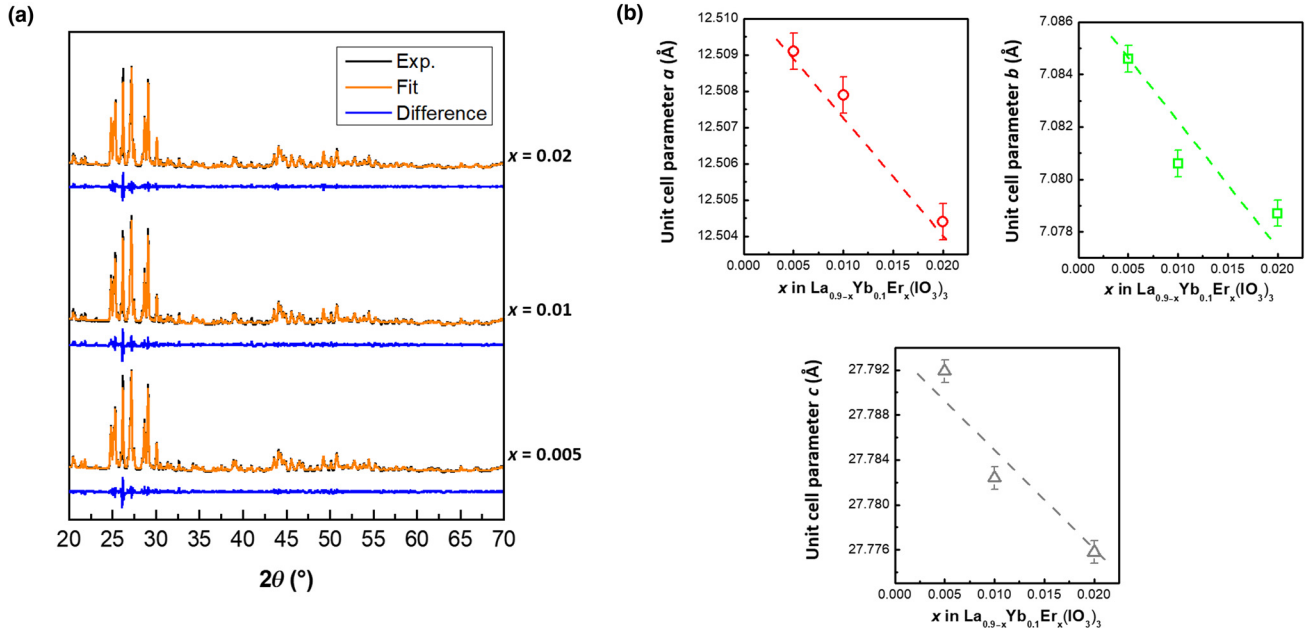


Figure 1. (a) PXRD diagrams of α-$La_{0.9-x}Yb_{0.1}Er_x(IO_3)_3$ for $x = 0.005$, 0.01, and 0.02 and their associated Le Bail fits. α-$La(IO_3)_3$ is a monoclinic phase, crystallizing in the Cc space group. (b) Evolution of the unit cell parameters *a*, *b*, and *c* as a function of *x* in α- $La_{0.9-x}Yb_{0.1}Er_x(IO_3)_3$.

$(IO_3)_3$ nanocrystals with Er^{3+} ions by La^{3+} substitution and showed that Er^{3+}-doped α-$La(IO_3)_3$ nanocrystals emit both UC-PL and SHG signals under 800- and 980-nm excitations. Here we report on multifunctional Yb^{3+},Er^{3+}-doped α-$La(IO_3)_3$ nanocrystals demonstrating optimized UC-PL properties and a strong SHG activity. In addition, because of the resonant conditions of UC-PL and the intrinsic non-resonant behavior of SHG in the material transparency range, special attention has been paid to a possible interplay between the two signals when the excitation wavelength is scanned around the Yb^{3+} and Er^{3+} absorption bands.

Results and discussion

Synthesis of α-$La_{1-y-x}Yb_yEr_x(IO_3)_3$ nanocrystals

α-$La_{1-y-x}Yb_yEr_x(IO_3)_3$ nanocrystals, with $y = 0.1$ and $x = 0.005$, 0.01, and 0.02, were synthesized using a microwave-assisted hydrothermal method, as reported in Ref. [19]. In the following, the nanocrystals will be referred to as α-$La_{0.9-x}Yb_{0.1}Er_x(IO_3)_3$. Briefly, $LaCl_3$, $YbCl_3$, $ErCl_3$, and HIO_3 precursors (all purchased from Sigma-Aldrich, France, purity >99.9%) were mixed in water and introduced into a quartz vessel, tightly sealed. The mixture was then heated through microwave radiations (power: 800 W) at 250 °C for 10 min. After cooling down (cooling rate: 10 °C/min), the obtained powders were washed with pure water and dried at room temperature. Nanocrystals were then mixed in ethylene glycol and sonicated for 15 min at a typical concentration of 0.1 mg/mL so as to obtain dispersions for the subsequent optical characterizations. Note that the quantity of inserted rare-earth ions inside the α-$La(IO_3)_3$ matrix is relatively large (>10 mol%) and that the term "doping" may not be strictly speaking the more appropriate. However, for the sake of consistency with this research field, it will be used throughout this paper.

Characterization of nanocrystal structure and morphology

Obtained α-$La_{0.9-x}Yb_{0.1}Er_x(IO_3)_3$ powders were characterized by powder x-ray diffraction (PXRD) using a Siemens D8 Advance diffractometer (Cu $K_{\alpha 1}$ radiation, 40 mA, 40 kV). Figure 1(a) shows the PXRD diagrams of $La_{0.9-x}Yb_{0.1}Er_x(IO_3)_3$ with $x = 0.005$, 0.01, and 0.02, along with their associated Le Bail refinements, based on already published results as input parameters (ICSD card #171250).[17] No phase impurity was detected. This is consistent with the results published by Taouti et al. on α-$La(IO_3)_3$ and by Suffren et al. on β-$La(IO_3)_3$ as both polymorphs can incorporate more than 10 mol% of Yb^{3+}.[18,22]

The unit cell parameters of $La_{0.9-x}Yb_{0.1}Er_x(IO_3)_3$ were obtained from the Le Bail fits and are shown in Fig. 1(b). As the concentration of Er^{3+} is raised, the unit cell parameters *a*, *b*, and *c* become smaller according to the Vegard's law. It is consistent with the decrease in the ionic radius from La^{3+} ($r_{La3+} = 1.216$ Å in a ninefold coordinated environment) to Er^{3+} ($r_{Er3+} = 1.062$ Å in a ninefold coordinated environment) and evidences the substitution of La^{3+} by Er^{3+} upon doping. In addition, the coherence length, L_c, of the crystalline domains obtained from the Le Bail fits assuming an isotropic broadening is about 60 ± 10 nm for each composition.

https://doi.org/10.1557/mrc.2019.137 Published online by Cambridge University Press

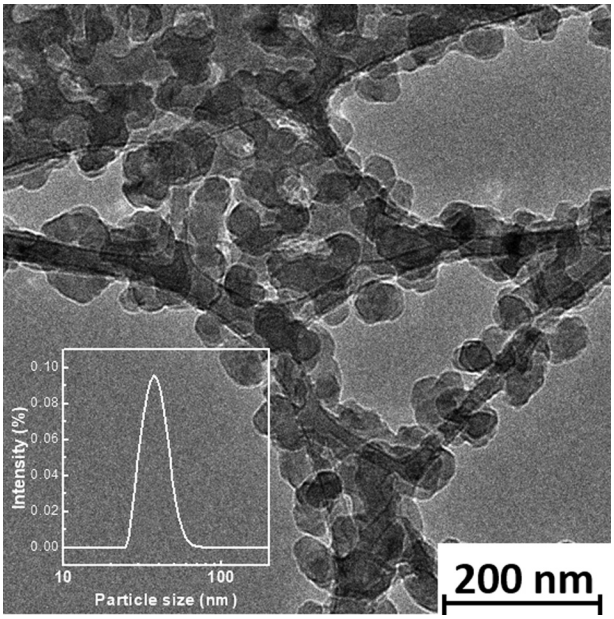


Figure 2. Typical TEM image of α-$La_{0.88}Yb_{0.1}Er_{0.02}(IO_3)_3$ nanocrystals recorded at 77 K. In the inset is shown the size distribution by intensity measured by DLS from $La_{0.88}Yb_{0.1}Er_{0.02}(IO_3)_3$ nanocrystals dispersed in ethylene glycol.

For $La_{0.9}Yb_{0.1}(IO_3)_3$, the values of the cell parameters can be derived through the extrapolation of the linear regression at $x = 0$ from Fig. 1(b). It results in $a = 12.5110(5)$ Å, $b = 7.0860(5)$ Å, and $c = 27.7965(5)$ Å. All these values are smaller than that of pure α-$La(IO_3)_3$ ($a = 12.526(2)$ Å, $b = 7.0939(9)$ Å, and $c = 27.823(4)$[17]) again in good agreement with the reduction of ionic radius from La^{3+} to Yb^{3+}($r_{Yb3+} = 1.042$ Å) and with the substitution of La^{3+} by Yb^{3+}.

The obtained α-$La_{0.9-x}Yb_{0.1}Er_x(IO_3)_3$ powders were dispersed in ethylene glycol using ultra-sound bath (for 15 min at room temperature). Dilute solutions were obtained by successive dilutions and drop-casted onto transmission electron microscopy (TEM) grids (Cu, 300 mesh, Electron Microscopy Sciences). After 4 days of drying at 80 °C to remove any trace of solvent, the carbon grids were inserted into a TEM (Philips CM300) operating at 300 kV and 77 K. Figure 2 shows a typical TEM image of α-$La_{0.88}Yb_{0.1}Er_{0.02}(IO_3)_3$, representative of all α-$La_{0.9-x}Yb_{0.1}Er_x(IO_3)_3$ compounds. One can observe that the nanocrystals are homogeneous in size, with a typical average size of 50 ± 10 nm. This value is consistent with the coherence length ($L_c = 60 \pm 10$ nm) previously determined and attests the single-crystal character of the obtained α-$La_{0.9-x}Yb_{0.1}Er_x(IO_3)_3$ nanocrystals. It is worth mentioning that, as previously reported in Ref. [19], doped and undoped α-$La(IO_3)_3$ nanocrystals present a strong affinity for the TEM carbon-coated Cu grids, resulting in a high coverage density.

In addition, dynamic light scattering (DLS) measurements performed from the ethylene glycol dispersions of α-$La_{0.9-x}Yb_{0.1}Er_x(IO_3)_3$ nanocrystals confirm the above-size estimations (TEM and PXRD) whatever the Er^{3+} concentration (inset in Fig. 2).

Evidence of multiple emission from α-$La_{0.9-x}Yb_{0.1}Er_x(IO_3)_3$ dispersions

The orientation-averaged optical properties of α-$La_{0.9-x}Yb_{0.1}Er_x(IO_3)_3$ nanocrystals dispersed in ethylene glycol were studied using the hyper-Rayleigh Scattering (HRS) configuration with a tunable (700–1300 nm) vertically polarized femtosecond Laser (Insight X3 Spectra-Physics, 80 MHz, 100–120 fs) as the excitation source.[19,21] Emitted signals were collected perpendicularly to the laser beam through a spectrometer (Andor Shamrock 193) coupled to a CCD camera (Andor iDus 401). The power-law dependences were obtained by adjusting the excitation power from 250 to 800 mW thanks to a half-wave plate associated with a polarizer cube. The peak intensity within the sample ranges from 0.5 to 1.6 GW/cm^2 and the average intensity from 4.5 to 13 kW/cm^2. Note that the peak intensity range is to be considered for the second harmonic scattering (SHS) process, whereas, the average intensity is assumed for the UC-PL signals since the typical excited state lifetime of Er^{3+} is of the order of several tens of μs, i.e., much longer than the excitation fs laser pulse.

All dispersions of α-$La_{0.9-x}Yb_{0.1}Er_x(IO_3)_3$ nanocrystals in ethylene glycol emit several characteristic optical signals corresponding to SHG and UC-PL, as illustrated in Fig. 3(a) for two resonant excitation wavelengths at 800 nm (red curve) and 980 nm (dark red curve). Arrows indicate the SHS signal whose position varies with the excitation wavelength, namely, $\lambda_{SHS} = 400$ nm for $\lambda_{exc} = 800$ nm and $\lambda_{SHS} = 490$ nm for $\lambda_{exc} = 980$ nm. In addition, the power-law dependence of the SHS intensity scales quadratically with the peak intensity as expected for SHS (Supplementary Fig. S1). The other characteristic peaks centered at 525, 550, and 660 nm are independent of the excitation wavelength and correspond to the UC-PL process through the well-known Er^{3+} electronic transitions. As reminded in Supplementary Fig. S2, the peaks at 525, 550, and 660 nm are associated with the $^2H_{11/2} \rightarrow {}^4I_{15/2}$, $^4S_{3/2} \rightarrow {}_4I_{15/2}$, and $^4F_{9/2} \rightarrow {}^4I_{15/2}$ transitions, respectively.[23,24] When plotted on logarithmic scales, the power-law dependence of the UC-PL intensity of each emission wavelength [Fig. 3(b)] scales as $I_\omega^{1.5}$ where I_ω is the average excitation intensity. For the UC-PL emission, the sequential absorption of n photons can lead to different values of the exponent according to the competition between the linear decay up-conversion processes.[25] The value here obtained at $n = 1.5$ is typical of the up-conversion processes in co-doped Yb^{3+},Er^{3+} systems under such excitation intensities.[24,26]

In terms of relative intensities between the SHS and UC-PL signals and after a proper calibration of the wavelength-dependent response of the experimental set-up,[21] the signals at 400, 525, and 550 nm are very similar under an excitation wavelength set at 800 nm and whatever the Er content ($x =$ 0.005, 0.01, and 0.02). However, when the resonant excitation

https://doi.org/10.1557/mrc.2019.137 Published online by Cambridge University Press

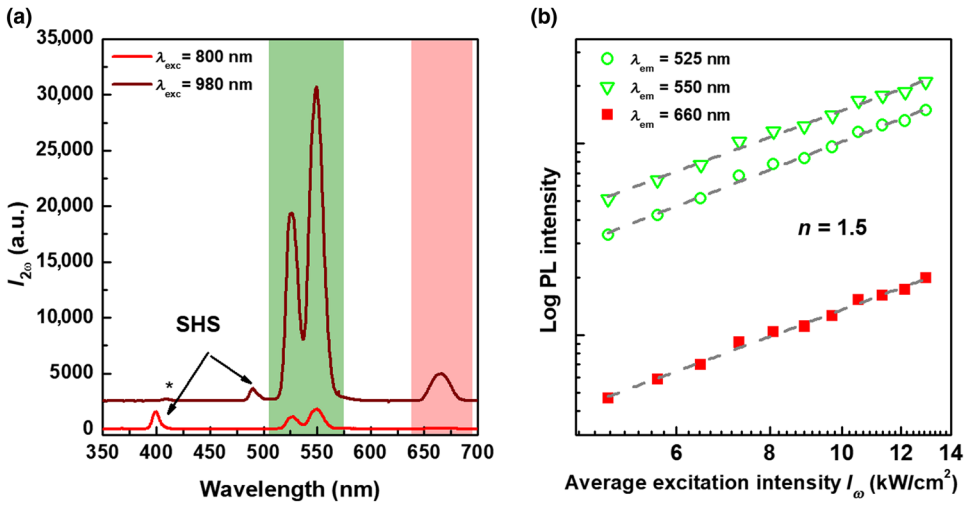


Figure 3. (a) Emission spectra of α-$La_{0.88}Yb_{0.1}Er_{0.02}(IO_3)_3$ nanocrystal dispersions in ethylene glycol under a 800-nm excitation (red curve) and a 980-nm excitation (dark red curve). For sake of clarity, the spectra have been stacked. The arrows point out the SHG signals, whereas the up-conversion emission is evidenced at 525, 550, and 660 nm. * is discussed in the text. (b) Power-law dependence of the UC-PL intensity at 525, 550, and 660 nm, in logarithmic scale under a 980-nm excitation. Data correspond to the symbols and dashed lines to the linear fit giving a slope of $n = 1.5$.

is shifted to 980 nm, a much more efficient UC process can be noticed comparatively to the almost constant SHS signal. Note that the overall spectral dependence of the SHS and UC-PL signals according to the excitation wavelength is further studied in the following section.

Spectral response of the SHS and UC-PL signals under resonant conditions

To understand better the evolution of SHS and UC-PL emissions with the excitation wavelength, the emission spectra of the α-$La_{0.88}Yb_{0.1}Er_{0.02}(IO_3)_3$ nanocrystals dispersed in ethylene glycol were recorded by scanning both in the 780–820 and 900–1020 nm ranges. After fitting of each characteristic peak with Gaussian functions, the UC-PL at 550 nm and SHS intensities are reported in Fig. 4. For both excitation ranges, the SHS signal appears rather constant with the excitation wavelength (Fig. 4, black curves). On the contrary, the UC-PL signal strongly depends on the excitation wavelength (Fig. 4, green curves). Such evolution of the UC-PL signal is directly correlated to the real absorption levels of Er^{3+} and Yb^{3+} whereas SHS only involves virtual states. In Fig. 4(a), the green curve corresponds to the typical absorption of Er^{3+} around 800 nm, namely to the $^4I_{15/2} \rightarrow {}^4I_{9/2}$ electronic transition.[27] In Fig. 4(b), the green curve is well correlated to the $^2F_{7/2} \rightarrow {}^2F_{5/2}$ transition of the Yb^{3+} excitation spectrum. Note also that the absorption cross-section of Er^{3+} around 980 nm

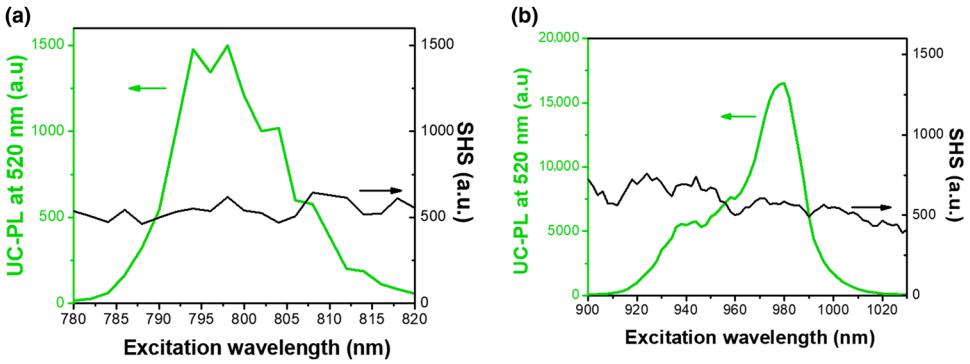


Figure 4. Spectral response of the emission intensity of the UC-PL at 550 nm (green curves) and SHG signals (black curves) in the 780–820 nm (a) and 900–1030 nm (b) ranges for α-$La_{0.88}Yb_{0.1}Er_{0.02}(IO_3)_3$ nanocrystals dispersed in ethylene glycol. These spectra were recorded for a peak intensity of 1 GW/cm. Note that for the sake of comparison of SHS and UC-PL intensity, both *y*-axis scales were kept identical in graph (a). On graph (b), as the UC-PL intensity is much more intense than SHS, the *y*-axis scales were chosen differently. It is possible to compare the absolute intensity values of the two graphs (a) and (b) as a thorough calibration of the set-up has been performed as the function of the excitation wavelength.[21]

https://doi.org/10.1557/mrc.2019.137 Published online by Cambridge University Press

is 10 times smaller than that of Yb^{3+} and thus Er^{3+} ions do not contribute to the excitation spectrum.[28] Hence, according to the excitation wavelength, two UC-PL mechanisms can be suggested:

- For an excitation at 980 nm, the UC-PL process first involves Yb^{3+} ions. After absorption of the incident photons to the $^2F_{5/2}$ excited state, energy is transferred to the neighboring Er^{3+} ions in their vicinity. Because of the long lifetime of the $^4I_{11/2}$ level of Er^{3+}, further energy transfer from Yb^{3+} is repeated (before de-excitation of Er^{3+}) thus allowing the population of higher excited states. A two-photon process thus results in the Er^{3+} PL emission at 525 and 550 nm from the $^2H_{11/2}$ and $^4S_{3/2}$ levels, respectively. In addition, a three-photon process from the $^2H_{9/2}$ is also observed as evidenced in Fig. 3(a) by the weak emission at ~400 nm.
- For an excitation at 800 nm, the UC-PL process occurs exclusively through the Er^{3+} ions, as Yb^{3+} shows no absorption in this range. Er^{3+} ions are first excited to the $^4I_{9/2}$ level before the absorption of a second photon populating higher excited states of Er^{3+} and leading to a PL emission from the $^2H_{11/2}$ and $^4S_{3/2}$ levels.

The highest conversion efficiency of the UC-PL process, illustrated in Fig. 3(a) for an excitation wavelength at 980 nm, is thus consistent with the absorption cross-section of Yb^{3+} which is known to be much larger than that of Er^{3+} at 800 nm.[29] Similarly, when Yb^{3+} is used as a sensitizer, a three-photon process with an emission at ~400 nm is only detectable when pumping at 980 nm.

Regarding the SHG conversion efficiency, the SHS signal is measured constant within the experimental uncertainties (evaluated at 15%[21]) (Fig. 4) while scanning in both excitation ranges (780–820 and 900–1020 nm). Hence, the SHG signal is not modulated in both excitation ranges, on the contrary to the UC-PL process which is strongly dependent on the excitation wavelength. Under such resonant excitation conditions for the Er^{3+} and Yb^{3+} ions, the absence of interplay between the SHS and UC-PL processes can be clearly noticed, indicating that the real transition levels of the lanthanide ions are not involved in the SHS emission. The absence of interplay here observed for the UC-PL and SHG processes might be attributed to the intrinsic properties of lanthanum iodate compounds themselves. Indeed, the SHG efficiency in iodate materials is mainly attributed to the stereoactive lone-pair of I^{5+},[30,31] whereas the PL comes from the lanthanide ions, substituting La^{3+} as evidenced by the PXRD results. Such a behavior would deserve further comparison with other non-centrosymmetric structures like $LiNbO_3$ for which co-doping with Er^{3+} and Yb^{3+} ions has already been achieved.

Conclusions

Microwave-assisted hydrothermal reaction allows to successfully produce α-$La_{0.9-x}Yb_{0.1}Er_x(IO_3)_3$ nanocrystals with x = 0.005, 0.01, and 0.02. Under NIR resonant excitations at around 800 and 980 nm, corresponding to the Er^{3+} and Yb^{3+} excited levels, a simultaneous emission of UC-PL and SHS signals can be observed. Very notably, Yb^{3+} acts as a strong sensitizer for the UC-PL at 980 nm and no competition between the two processes (UC-PL and SHS) could be evidenced in the co-doped lanthanide iodate nanocrystals.

Supplementary material

The supplementary material for this article can be found at https://doi.org/10.1557/mrc.2019.137.

Acknowledgments

The authors thank the French-Swiss Interreg V and French ANR programs for financial supports (Projects OncoNanoscreen and Racine) and the 2015−2020 French Contrat Plan État Région (project E-TIME, SYMME).

References

1. K. Wang, X. He, X. Yang, and H. Shi: Functionalized silica nanoparticles: a platform for fluorescence imaging at the cell and small animal levels. *Acc. Chem. Res.* **46**, 1367 (2013).
2. C. Bouzigues, T. Gacoin, and A. Alexandrou: Biological applications of rare-earth based nanoparticles. *ACS Nano* **5**, 8488 (2011).
3. O. Faklaris, D. Garrot, V. Joshi, F. Druon, J.P. Boudou, T. Sauvage, P. Georges, P.A. Curmi, and F. Treussart: Detection of single photoluminescent diamond nanoparticles in cells and study of the internalization pathway. *Small* **4**, 2236 (2008).
4. O.S. Wolfbeis: An overview of nanoparticles commonly used in fluorescent bioimaging. *Chem. Soc. Rev.* **44**, 4743 (2015).
5. S. Gigan: Optical microscopy aims deep. *Nat. Photonics* **11**, 14 (2017).
6. G. Dantelle, M. Matulionyte, D. Testemale, A. Cantarano, A. Ibanez, and F. Vetrone: Nd^{3+}-doped $Gd_3Sc_2Al_3O_{12}$ nanocrystals: towards efficient nanoprobes for temperature sensing. *Phys. Chem. Chem. Phys.* **21**, 11132 (2019).
7. B. del Rosal, U. Rocha, E.C. Ximendes, E. Martín Rodríguez, D. Jaque, and J. García Sol: Nd^{3+} ions in nanomedicine: perspectives and applications. *Opt. Mater.* **63**, 185 (2017).
8. R. Wang, X. Li, L. Zhou, and F. Zhang: Epitaxial seeded growth of rare-earth nanocrystals with efficient 800 nm near-infrared to 1525 nm short-wavelength infrared downconversion photoluminescence for in vivo bioimaging. *Angew. Chem. Int. Ed.* **53**, 12086 (2014).
9. M. Tan, B. del Rosal, Y. Zhang, E. Martín Rodríguez, J. Hu, Z. Zhou, R. Fan, D.H. Ortgies, N. Fernández, I. Chaves-Coira, Á Núñez, D. Jaque, and G. Chen: Rare-earth-doped fluoride nanoparticles with engineered long luminescence lifetime for time-gated in vivo optical imaging in the second biological window. *Nanoscale* **10**, 17771 (2018).
10. S. Chinnathambi and N. Shirahata: Recent advances on fluorescent biomarkers of near-infrared quantum dots for in vitro and in vivo imaging. *Sci. Technol. Adv. Mater.* **20**, 337 (2019).
11. L. Mayer, G. Dantelle, V. Jacques, S. Perruchas, G. Patriarche, J.F. Roch, and T. Gacoin: Dual light emitting nanoparticles: second harmonic generation combined with rare-earth photoluminescence. *J. Mater. Chem. C* **2**, 7681 (2014).
12. P. Pantazis, J. Maloney, D. Wu, and S.E. Fraser: Second harmonic generating (SHG) nanoprobes for in vivo imaging. *PNAS* **107**, 14535 (2010).
13. D. Staedler, T. Magouroux, R. Hadji, C. Joulaud, J. Extermann, S. Schwung, S. Passemard, C. Kasparian, G. Clarke, M. Gerrmann, R. Le Dantec, Y. Mugnier, D. Rytz, D. Ciepielewski, C. Galez, S. Gerber-Lemaire, L. Juillerat-Jeanneret, L. Bonacina, and J.-P. Wolf: Harmonic Nanocrystals for biolabeling: a survey of optical properties and biocompatibility. *ACS Nano* **63**, 2542 (2012).
14. L. Dubreil, I. Leroux, M. Ledevin, C. Schleder, L. Lagalice, C. Lovo, R. Fleurisson, S. Passemard, V. Kilin, S. Gerber-Lemaire, M.-A. Colle, L.

https://doi.org/10.1557/mrc.2019.137 Published online by Cambridge University Press

Bonacina, and K. Rouger: Multi-harmonic imaging in the second near-infrared window of nanoparticle-labeled stem cells as a monitoring tool in tissue depth. *ACS Nano* **117**, 6672 (2017).
15. E. Slenders, H. Bove, M. Urbain, Y. Mugnier, A. Yasin Sonay, P. Pantazis, L. Bonacina, P. Vanden Berghe, M. vandeVen, and M. Ameloot: Image correlation spectroscopy with second harmonic generating nanoparticles in suspension and in cells. *J. Phys. Chem. Lett.* **9**, 6112 (2018).
16. X.L. Le, C. Zhou, A. Slablab, D. Chauvat, C. Tard, S. Perruchas, T. Gacoin, P. Villeval, and J.F. Roch: Photostable second-harmonic generation from a single $KTiOPO_4$ nanocrystal for nonlinear microscopy. *Small* **4**, 1332 (2008).
17. K.M. Ok and P.S. Halasyamani: New metal iodates: syntheses, structures, and characterizations of noncentrosymmetric $La(IO_3)_3$ and $NaYI_4O_{12}$ and centrosymmetric β-$Cs_2I_4O_{11}$ and $Rb_2I_6O_{15}(OH)_2{\cdot}H_2O$. *Inorg. Chem.* **44**, 9353 (2005).
18. M.B. Taouti, Y. Suffren, O. Leynaud, D. Benbertal, A. Brenier, and I. Gautier-Luneau: Structures, thermal behaviors, and luminescent properties of anhydrous lanthanum iodate polymorphs. *Inorg. Chem.* **54**, 3608 (2015).
19. S. Regny, J. Riporto, Y. Mugnier, R. Le Dantec, S. Kodjikian, S. Pairis, I. Gautier-Luneau, and G. Dantelle: Microwave synthesis and up-conversion properties of SHG-active α-$(La,Er)(IO_3)_3$ Nanocrystals. *Inorg. Chem.* **58**, 1647 (2019).
20. C. Joulaud, Y. Mugnier, G. Djanta, M. Dubled, J.C. Marty, C. Galez, J.P. Wolf, L. Bonacina, and R. Le Dantec: Characterization of the nonlinear optical properties of nanocrystals by hyper Rayleigh scattering. *J. Nanobiotechnol.* **11**, S8 (2013).
21. J. Riporto, M. Urbain, Y. Mugnier, V. Multian, F. Riporto, K. Bredillet, S. Beauquis, C. Galez, V. Monnier, Y. Chevolot, V. Gayvoronsky, L. Bonacina, and R. Le Dantec: Second harmonic spectroscopy of ZnO, $BiFeO_3$ and $LiNbO_3$ nanocrystals. *Opt. Mater. Express* **9**, 1955 (2019).
22. Y. Suffren, O. Leynaud, P. Plaindoux, A. Brenier, and I. Gautier-Luneau: Differences and similarities between lanthanum and rare-earth iodate anhydrous polymorphs: structures, thermal behaviors, and luminescent properties. *Inorg. Chem.* **55**, 11264 (2016).
23. G.H. Dieke: *Spectra and Energy Levels of Rare Earth Ions in Crystals* (Interscience Publishers, New York, NY, USA, 1968).
24. P.S. Peijzela, A. Meijerink, R.T. Wegh, M.F. Reid, and G.W. Burdick: A complete 4f n energy level diagram for all trivalent lanthanide ions. *J. Solid State Chem.* **178**, 448 (2005).
25. M. Pollnau, D.R. Gamelin, S.R. Lüthi, H.U. Güdel, and M.P. Hehlen: Power dependence of upconversion luminescence in lanthanide and transition-metal-ion systems. *Phys. Rev. B* **61**, 3337 (2000).
26. J.F. Suyver, A. Aebischer, S. García-Revilla, P. Gerner, and H.U. Güdel: Anomalous power dependence of sensitized upconversion luminescence. *Phys. Rev. B* **71**, 125123 (2005).
27. G. Blasse and B.C. Grabmaier: *Luminescent Materials* (Springer-Verlag, Berlin Heidelberg, 1994).
28. F. Huang, X. Liu, Y. Ma, S. Kang, L. Hu, and D. Chena: Origin of near to middle infrared luminescence and energy transfer process of Er^{3+}/Yb^{3+} co-doped fluorotellurite glasses under different excitations. *Sci. Rep.* **5**, 8233 (2015).
29. H. Dong, L.D. Sun, and C.H. Yan: Energy transfer in lanthanide upconverting studies for extended optical applications. *Chem. Soc. Rev.* **44**, 1608 (2015).
30. H.-Y. Chang, S.-H. Kim, P.S. Halasyamani, and K.M. Ok: Alignment of lone pairs in a new polar material: synthesis, characterization, and functional properties of $Li_2Ti(IO_3)_6$. *J. Am. Chem. Soc.* **131**, 2426 (2009).
31. C.F. Sun, C.L. Hua, and J.G. Mao: $PbPt(IO_3)_6(H_2O)$: a new polar material with two types of stereoactive lone-pairs and a very large SHG response. *Chem. Commun.* **48**, 4220 (2012).

https://doi.org/10.1557/mrc.2019.137 Published online by Cambridge University Press